aerospace

Article

# Can the Orbital Debris Disease Be Cured Using Lasers?

**Stefan Scharring * and Jürgen Kästel**

Institute of Technical Physics, German Aerospace Center (DLR), Pfaffenwaldring 38–40, 70569 Stuttgart, Germany; juergen.kaestel@dlr.de
* Correspondence: stefan.scharring@dlr.de

**Abstract:** Ground-based high-power lasers are, in principle, able to de-orbit any kind of space debris object from the low Earth orbit (LEO) by remotely inducing laser-ablative momentum. However, the assessment of efficiency and operational safety depends on many factors, like atmospheric constraints or the risk of debris disintegration during irradiation. We analyze laser momentum for a great variety of target geometries and sizes and—for the first time in a large-scale simulation—include thermal constraints in the laser irradiation configuration. Using a coherently coupled 100 kJ laser system at 1030 nm wavelength and a 5 ns pulse duration in an optimized pointing elevation angle range, the pulse frequency should amount to less than 10 Hz to prevent fragment meltdown. For mechanically intact payloads or rocket bodies, repetition rates should be even lower. Small debris fragments sized between 10 and 40 cm can be de-orbited by employing around 100 to 400 station passes with head-on irradiation, while objects exceeding 2 m typically require far more than 1000 irradiations for de-orbit. Hence, laser-based debris removal cannot be considered a prime space sustainability measure to tackle the highest-risk large debris, yet it can provide the remediation of a multitude of small-sized debris using small networks of globally distributed laser sites.

**Keywords:** space debris; space sustainability; Kessler syndrome; debris removal; high-energy lasers; laser pulse repetition rate; laser ablation; laser momentum transfer; laser-induced heating; thermo–mechanical integrity

check for updates

**Citation:** Scharring, S.; Kästel, J. Can the Orbital Debris Disease Be Cured Using Lasers? *Aerospace* **2023**, *10*, 633. https://doi.org/10.3390/aerospace10070633

Academic Editor: John Sinko

Received: 23 May 2023
Revised: 3 July 2023
Accepted: 5 July 2023
Published: 13 July 2023

## 1. Introduction

As an update to the usually cited prediction [1] of a possibly exponential future increase in space debris in the low Earth orbit (LEO), known as the Kessler syndrome, which would massively endanger or even shut down space operations, the onset of this phenomenon in highly frequented altitudes around the sun-synchronous orbit has recently been reported [2]. This fact induces a paradigm shift in space situational awareness from being a sustainability issue to an emergency question. In a certain regard, this is also reflected in the report recently issued by the U.S. National Aeronautics and Space Administration (NASA) [3], re-assessing the use of ground-based or space-based lasers for the removal of a multitude of small space debris objects as possibly being the most efficient way to tackle the scope of space debris remediation at present. Of course, the current efforts like Clearspace-1 [4] or Active Debris Removal by Astroscale-Japan (ADRAS-J) [5] for removing inactive payloads or spent upper stages as possible sources of new fragments due to collisions and/or explosions are an adequate measure in terms of the appropriate long-term solution for the sustainability of the space debris environment. Nevertheless, the increasing severity of—symbolically speaking—the symptoms of the orbital debris disease, i.e., the fragmentation of debris and the orbit's congestion through space debris, puts into question the prevailing limitation of interest for debris-removal activities to only a few "pathogens", i.e., payloads and rocket bodies, per year [6].

On top of ongoing debris fragmentation dynamics, the Kessler syndrome is currently on the verge of becoming evident also in terms of increasing debris awareness. Improving optical performance for detection and tracking allows for the cataloging of more and more small objects, which are more prevalent the smaller they are [7]. Moreover, the rise of mega-constellations is anticipated to increase the number of collision warnings in the low Earth orbit by more than two orders of magnitude [8]. In combination, the future burden of collision avoidance in space debris management might encounter critical capacity limits, which renders the removal of a multitude of objects a welcome option for short-term mitigation, even if it contributes less to the space environment from a sustainability perspective. In this regard, methods for active debris removal (ADR) that comprise dedicated in-orbit missions for the manipulation of specific objects using, e.g., nets, electrodynamic tethers, ion beams, or robotic arms [9], appear unsuitable for de-orbiting a multitude of small debris. For these, so-called sweepers have been proposed in various conceptions, orbiting with large material pads for the deceleration, break-up, or capture of small debris [3]. Alternatively, as a non-contact method that can be operated remotely over great distances, recoil from the high-power laser ablation of the debris' surfaces has been analyzed in various regards as a method to de-orbit debris objects for atmospheric burn-up in a stepwise manner.

Since the first proposals, dating from the 1990s, both ground-based [10] and space-based [11] high-power lasers have been investigated regarding their advantages and drawbacks in the field of laser-based space debris removal. Space-based operation facilitates fairly relaxed constraints on the engineering of beam-focusing units, benefiting from reduced distances and the possible usage of short laser wavelengths [12]; however, it requires a very compact and efficient laser unit [13] for space-qualified operations in a harsh environment without opportunities for on-site maintenance. In comparison, ground-based laser stations benefit from a comprehensive infrastructure covering extensive power supply, tightly supervised operation, and flexible maintenance without a significant need for constraining the volume or mass of the laser site, which gave rise to the proposal of technology from large high-energy laser facilities as blueprints for possible removal lasers [14].

Considering the existing limitations of currently available laser power, some concepts include the irradiation of small debris via multiple station passes for stepwise de-orbiting [15] instead of removing the object by means of a single pass irradiation. But even under very optimistic assumptions of the future power scaling of high-energy lasers, laser-ablative momentum transfer to space debris is not limitless: the laser-induced thermal disintegration of space debris targets— initially experimentally observed in [11] but afterward neglected in the literature for decades—recently emerged as a constraint to ensure operational safety [16], underpinned by the experimental proof of solar cell fragmentation from pulsed laser irradiation in a relevant parameter range [17]. In this regard, it is no wonder that laser-based removal or even the nudging of space debris is frequently associated with its potential dual use for applying directed energy as a threat to satellites [18,19]. Therefore, in our study, we consider the irradiation level that presumably may not be crossed in order to maintain the integrity of the irradiated debris object, which may serve as a first proxy to assess the threat level of a debris removal laser station. We hope that this approach helps the acquisition of a clearer and more realistic picture of the potential and implications that the research and development of laser-based technologies for the ground-based removal of space debris might hold.

## 2. Methods

A brief overview of the computational workflow of this study can be seen in Figure 1. We analyzed the orbit modification of a space debris object through recoil from surface ablation induced by repetitively pulsed laser irradiation from a high-energy laser station on the ground. Head-on irradiation at rather low elevation angles (see Figure 1a) was compared to outward irradiation near the zenith (Figure 1b) in terms of velocity change $\Delta v$ and laser-induced temperature change $\Delta T$. The laser fluence $\Phi_{\mathrm{T}}$, arriving at the momentary debris position, was computed from the laser pulse energy $E_{\mathrm{L}}$, considering the distance $z$ between laser and debris with respect to the object's orbit altitude $h$ and its current zenith angle $\zeta$ or elevation angle $\varepsilon$, respectively. The impact of the transmitter design and atmospheric extinction, as well as turbulence compensation on $\Phi_T(t)$, is outlined in Section 2.1.

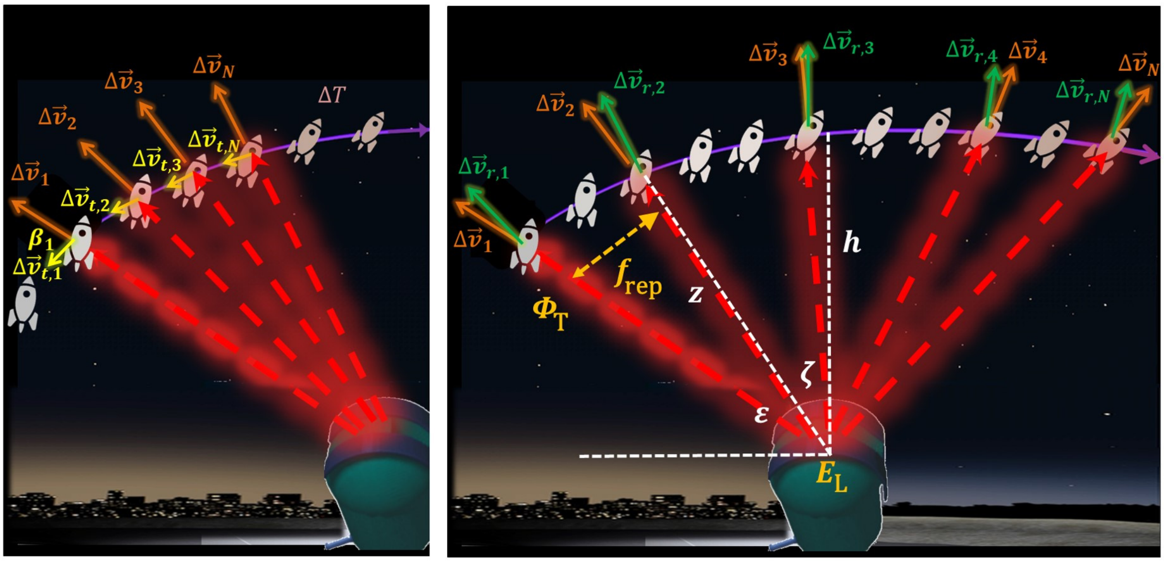

(**a**) (**b**)

**Figure 1.** Scheme of repetitively pulsed laser irradiation of space debris by a high energy laser ground station for perigee lowering by (**a**) head-on momentum and, alternatively, (**b**) outward momentum.

As a realistic computational input for the momentum-generation process of laser ablation, the dependencies of the momentum coupling coefficient $c_m = \Delta p / E_L$ and the coefficient of residual heat $\eta_{res} = \Delta Q / E_L$ on the incident fluence $\Phi_T$ are discussed in Section 2.2. Here, $\Delta p$ are the imparted momentum, $\Delta Q$ the laser-induced heat remaining in the debris object after ablation, and $A$ the irradiated area.

Section 2.3 gives an overview of the different debris target categories and geometries used in the raytracing computations of laser-imparted momentum and analytic estimates of laser-induced heat, as described in Section 2.4. Finally, the role of the laser-induced velocity change in orbit modification and de-orbiting is outlined in Section 2.5.

### 2.1. High-Energy Laser Ground Station

As a conceivable laser source for debris removal, we assumed a system of multiple laser emitters with comparably low pulse energy organized for coherent beam coupling as a phased array in a tiled aperture configuration. Based on the experimental work of our group outlined in [20], each of the single emitters was anticipated as diode-pumped Yb:YAG (Ytterbium-doped yttrium aluminum garnet) laser source in a master oscillator power amplifier configuration (MOPA) in which an initial laser pulse energy of 100 mJ is amplified within two stages up to an overall pulse energy of 20 J with a pulse length of $\tau = 5$ ns at a wavelength of $\lambda = 1030$ nm, and a superior beam quality of $M^2 = 1.5$. The arrangement of 5000 of such emitters in a tiled aperture configuration [21] would allow for coherent beam coupling, yielding an overall laser pulse energy of $E_L = 100$ kJ.

For the beam transmission, we assumed an optical aperture with a diameter of $D_T = 4$ m and an initial radius of the effective laser beam of $w_0 = 0.715 \cdot D_T/2$, which corresponds to a 2% power loss at the transmitter from intensity clipping at the aperture edge. The ground station was anticipated to be operated in junction with an optical system for target acquisition and continuous laser tracking of the debris object during its station pass, exhibiting a low tracking uncertainty of $\sigma_t = 0.1$ arcsec enabled by adaptive optics and laser guide star (LGS) usage in the downlink from the object [22]. This allows for the needed high-precision pointing of the high-energy laser beam while the real-time data from ranging can be used to dynamically adapt the focus length of the transmitter to achieve a focus of the beam at the actual range of the debris object throughout the entire pass.

Turbulence compensation is not only required for the downlink but also for the uplink, i.e., power beaming to the debris object, in particular at greater distances [23]. Hence, an additional LGS was employed, which is assumed to point slightly ahead of the debris object and probe the turbulence in the solid angular segment relevant to the uplink path. Real-time data analysis of corresponding measurements with a Shack–Hartmann sensor on the ground allows for dynamic conjugation of turbulence-induced phase distortions by actively shifting the phases of the different laser emitters based on data from heterodyne phase detection. The overall performance of such a beam transmission system can be quantified by the Strehl ratio $Str$ [24] yielding the following expression for the laser spot radius $w$ focused at the distance $z$ from the transmitter:

$$w(z) = \frac{M^2 \cdot \lambda \cdot z}{\pi \cdot w_0 \cdot \sqrt{Str}}. \tag{1}$$

Here, the Strehl ratio comprises the temporal compensation, the so-called cone effect, and a spatial contribution expressed as

$$Str = S_{\mathrm{temp}} \cdot S_{\mathrm{cone}} \cdot S_{\mathrm{zonal}}. \tag{2}$$

Specifically, the factor $S_{\mathrm{temp}}$ quantifies temporal de-correlation effects and is given by

$$S_{\mathrm{temp}} = \exp\left[-\left(f_G / f_{3\mathrm{dB}}\right)^{5/3}\right] \tag{3}$$

where $f_G$ is the Greenwood frequency and $f_{3\mathrm{dB}} = 300$ Hz is the characteristic response frequency of the phase correction system. Likewise, the factor $S_{\mathrm{cone}}$ considers the residual atmospheric volume not covered by LGS probing:

$$S_{\mathrm{cone}} = \exp\left[-\left(D_{\mathrm{T}} / d_0\right)^{5/3}\right] \tag{4}$$

where $d_0$ is a parameter describing focus anisoplanatism. Moreover, a spatial contribution $S_{\mathrm{zonal}} \approx 0.9$ was employed stemming from the spatial configuration of the phase compensation in the tiled aperture array. Since $f_G$ and $d_0$ depend on the underlying turbulence model and, in the case of $f_G$, on the propagation length, $Str$ is a function of both orbit altitude $h$ and beam-pointing zenith angle $\zeta$, cf. [22] for a detailed description.

The residual impact of atmospheric turbulence beam pointing in tip-tilt correction mode has been assessed following [25], providing a pointing jitter from $\sigma_{\mathrm{p}} = 0.17$ arcsec at zenith up to $\sigma_{\mathrm{p}} = 0.63$ arcsec at $\zeta = 65°$. Regarding extinction, we have employed data from [26] for clear air at $\lambda = 1.06$ µm showing an atmospheric transmissivity of $T = 86.6\%$ at zenith down to $T = 71.1\%$ at $\zeta = 65°$. Moreover, from practical considerations on the tiled aperture concept, we deemed the far-field power-in-the-bucket (discarding the side lobes) to be around $S_{PIB} \approx 65\%$ of the transmitted laser energy (including losses at the transmitter), which gives an overall amount of usable transmitted laser pulse energy of

$$E_{\mathrm{T}} = T(\zeta) \cdot S_{\mathrm{PIB}} \cdot E_{\mathrm{L}} \tag{5}$$

provided at the target's position in orbit as a spot with a radius given by $w(z)$.

### 2.2. Laser–Matter Interaction

For the computation of laser-based orbit modification, we employed the commonly used momentum coupling coefficient $c_m$

$$c_m = \Delta p / E_{\mathrm{inc}} \tag{6}$$

where $\Delta p$ is the momentum change of the target due to recoil obtained from the ablation jet and $E_{\text{inc}}$ is the laser pulse energy that hits the target.

Though the predominant fraction of the laser-induced heat leaves the target with the plasma jet formed by heated surface material, a residual amount of heat remains in the vicinity of the ablation zone after the ablation process and subsequently dissipates into the bulk. This phenomenon can be quantified using the residual heat coefficient $\eta_{res}$ by

$$\eta_{res} = \Delta Q / E_{\text{inc}} \tag{7}$$

where $\Delta Q$ is the amount of residual heat left in the target.

These coefficients of thermal and mechanical coupling, $c_m$ and $\eta_{res}$, are material-specific and depend on laser parameters such as wavelength $\lambda$ and pulse duration $\tau$. Moreover, both figures of merit show strongly non-linear behavior regarding their dependency on the incident laser fluence $\Phi$, which should be considered for a realistic simulation of a laser-based orbit-modification maneuver. Taking this into account, we use a parametric fit function of $c_m(\Phi)$ based on experimental data for aluminum and stainless steel as relevant target materials [27]. The pronounced dependency of $c_m$ on the incident laser fluence $\Phi$ can be seen from the respective data shown in Figure 2a. Experimental data from [28] has been extracted using the software Image-J, and an empirical fit function has been applied. The corresponding fit parameters, cf. [29], serve as an input for momentum coupling computations in the raytracing simulations of laser–matter interaction described below.

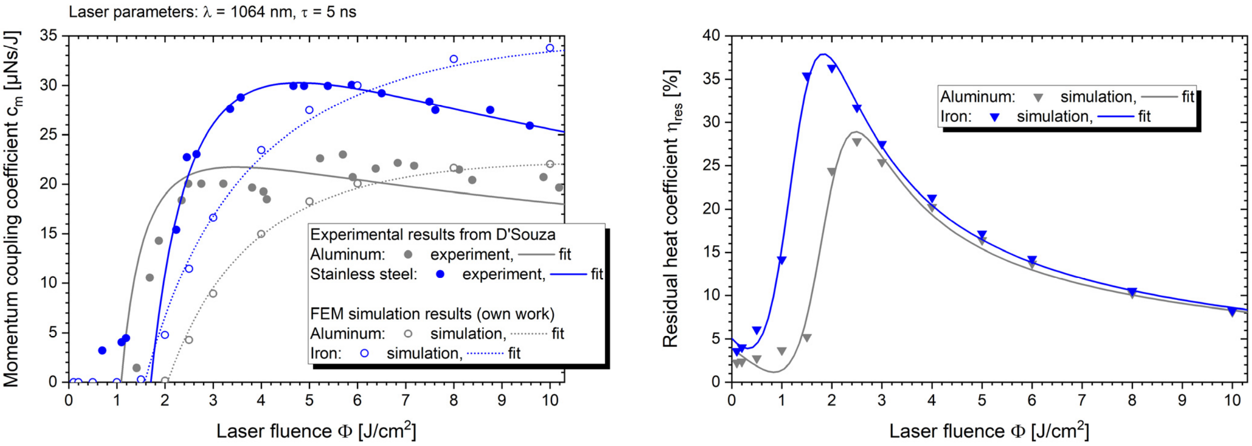

(**a**) (**b**)

**Figure 2.** (**a**) Momentum coupling as a function of incident fluence of a laser pulse with $\tau = 5$ ns pulse duration at $\lambda = 1064$ nm wavelength, which is close to the wavelength of our laser configuration (1030 nm). Experimental data from [28] has been reprinted with permission of the author (Copyright 2007 by Ch.B. D'Souza). The data is shown together with own simulation results for aluminum, stainless steel, and iron as well as corresponding data fits using the empirical fit function for $c_m(\Phi)$ derived in [30]. (**b**) Results from finite-elements-method (FEM) simulations on thermal coupling in laser ablation of aluminum and iron, respectively, for these laser parameters.

Beyond momentum coupling, laser-induced heat from repetitive laser ablation is of interest regarding possible limitations of laser-based removal. However, corresponding experimental data for the residual heat coefficient $\eta_{res}$ was not available for the experiments described in [28]. Instead, we have used results from our own simulations of the laser ablation process, implemented in the commercial finite-elements-method (FEM) software COMSOL Multiphysics$^{®}$ version 6.1, employing a modeling approach that has been developed in [31], and extended in further research. It is comprised of laser-induced heat transfer, evaporation cooling, material ablation, Knudsen layer formation, ablation plume gas dynamics, and plasma shielding.

As a preliminary validation for the scope of this work, the results of simulations that used the same laser parameters as had been reported from the experiments [28] are shown in Figure 2a (hollow symbols, dotted fit). Basically, despite the efforts we have put into our simulation setup, some discrepancies between experimental data and simulation results prevail: most notably, results for the ablation threshold of aluminum differ by a factor of two. We nevertheless deem this acceptable for our purposes since experimental data from the literature shows significant uncertainties as well: while for aluminum, we find $\Phi_0 = 1.1\,\mathrm{J/cm^2}$ at $\tau = 5$ ns [28], $3.2\,\mathrm{J/cm^2}$ at 6 ns [32], and $1.5\,\mathrm{J/cm^2}$ at 8 ns [33], the scatter with stainless steel is even larger exhibiting $\Phi_0 = 1.7\,\mathrm{J/cm^2}$ at $\tau = 5$ ns [28], $\Phi_0 = 7.3\,\mathrm{J/cm^2}$ at $\tau = 6$ ns [32], and $\Phi_0 = 0.8\,\mathrm{J/cm^2}$ at $\tau = 10$ ns [34], which shows a notable scatter of values, whereas one would actually expect $\Phi_0 \propto \sqrt{\tau}$ [32].

Moreover, the decrease in $c_m$ due to plasma shielding is predicted at higher fluences (not shown) in the simulations than reported from the experiment. While there is still room for improving the simulation setup regarding a more convincing match with experimental data, the overall rather good agreement of $c_m$ data between simulation and experiment in the relevant fluence range make us sufficiently confident to use empirical fits of simulation data of $\eta_{res}$, cf. Figure 2b, for this study, in order to derive a first estimate on thermal limitations in laser-based removal of space debris.

### 2.3. Space Debris Simulation Targets

For our simulations, we have chosen four different categories of cataloged debris objects: (i) 1000 fragments from explosions and collisions with a mass ranging from 1 kg to 50 kg, (ii) 100 medium-sized payloads from 50 kg to 1000 kg, (iii) a representative selection of 10 large-risk rocket bodies with high priority for ADR according to [35] exhibiting a mass between 1000 kg and 10,000 kg, and (iv) Envisat, listed as a high-risk object in [35], which is the largest known debris satellite in LEO. Fragments and medium-sized payloads have been selected from a larger debris population in LEO as of 2 July 2019, comprising objects at mean altitudes between 579 and 1179 km with an orbital eccentricity up to 0.2 and an orbit inclination between 65° and 110°. Orbital data had been retrieved from the catalog of the United States Strategic Command (USSTRATCOM) [36]. Data on mass and geometry have been provided from the Database and Information System Characterizing Objects in Space (DISCOS) of the European Space Agency (ESA) [37], in particular allowing us to derive geometric primitives for our simulations, cf. [22] for a description in greater detail. The scatterplot in Figure 3, which shows the ratios of the geometric X- and Y-axes, underlines the great variety of the investigated debris objects.

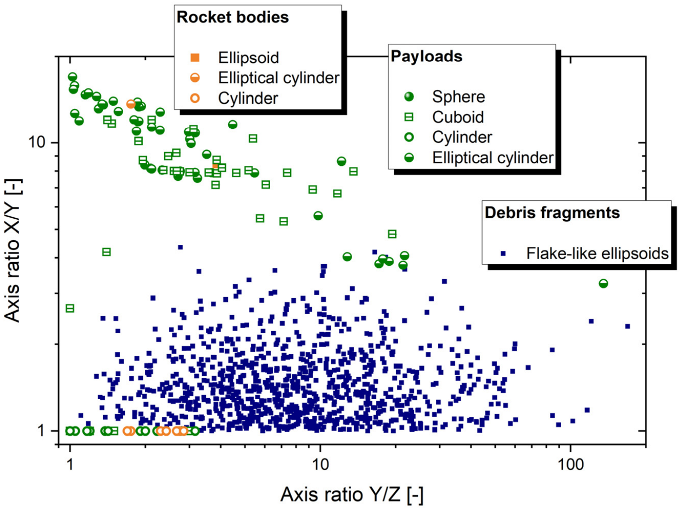

**Figure 3.** Axis ratios of debris simulation targets. Dimensions X, Y, and Z are defined according to the method of shadow dimensions as described in [38].

Aluminum is attributed as the surface material of the 101 payloads, while the outer shells of the rocket bodies are assumed to consist of stainless steel. Correspondingly, steel is also assumed as the material of choice for the 287 rocket fragments, whereas for the remaining 713 payload fragments, among which 342 have arisen from tests of kinetic anti-satellite weapons (ASAT tests), aluminum is selected as simulation material for laser–matter interaction.

### *2.4. Laser-Imparted Momentum and Heat*

For the computation of momentum from laser ablation, we have employed our numerical code EXPEDIT (Examination Program for Irregularly Shaped Debris Targets) [30], which is based on Liedahl's area-matrix approach [39]. It allows the consideration of arbitrarily oriented target surface elements and the quantification of corresponding implications on local fluence, momentum magnitude, and momentum direction. The simulation input in terms of the required dependency of momentum coupling on the fluence is taken from the parametric fit functions, cf. [29], of the experimental data shown in Figure 2a.

In our simulations, the laser intensity profile at the target range was positioned next to the target and assumed to exhibit a Gaussian fluence distribution that equals one of the focused laser spots. This allows for raytracing simulations with parallel rays to cover the "end-ballistics" of the irradiation. The beam waist $w(z)$ is given by Equation (1) and the spatial resolution of the single rays is $\Delta r = 0.02 \cdot w(z)$ yielding a fine discretization for momentum computation. The overall laser pulse energy is given by $E_{\mathrm{T}}$ as from Equation (5).

For our study, we assumed that the target orientation at the time of a laser pulse is unknown. To account for this, we used a Monte Carlo approach, similar to our study on photon pressure [22], which facilitated the sampling of the computed momentum for various orientations of the object. The attitude was parameterized by Eulerian angles, which were determined from a random uniform distribution. Moreover, we also included fluctuations of the offset between the laser spot center and the target's center of mass, denoted here as hit uncertainty, $\sigma_{\mathrm{h}}$, into the Monte Carlo sampling. The hit uncertainty can be derived from the tracking uncertainty $\sigma_{\mathrm{t}}$, the inherent beam pointing jitter $\sigma_{\mathrm{p}}$, cf. Section 2.1, and the distance to target as $\sigma_{\mathrm{h}} = z\sqrt{\sigma_{\mathrm{p}}^2 + \sigma_{\mathrm{t}}^2}$. The overall jitter $\sigma_{\mathrm{h}}$ then serves as the standard deviation of the Gaussian random distribution from which we determined the particular beam offset of the different Monte Carlo samples. For the polar angle of the offset's position vector, a uniform random distribution was employed, yielding overall five degrees of freedom for attitude and position of the debris object within the beam.

Using these definitions of random-beam offset and arbitrary target orientation, Monte Carlo sampling has been undertaken for each target at its particular altitude under twelve different beam-pointing zenith angles $\zeta$ ranging from $0^\circ$ to $65^\circ$ in steps of $\Delta\zeta = 5^\circ$ unless the spot's peak fluence fell below the material's ablation threshold. Sampling was halted when the averaged momentum achieved convergence after at least 11 samples or, in the case of slowly converging samples, 1000 samples had been computed. Eventually, 15,257 Monte Carlo simulations comprising an overall number of 9,130,275 samples of raytracing-based momentum computations were employed to establish a target- and altitude-specific database of averaged values of laser-imparted momentum as a function of the beam-pointing zenith angle.

Note that in the following, only the momentum component $\Delta p_{ax}$ co-axial to the laser beam propagation axis was employed, whereas the component perpendicular to the beam axis was discarded since those components should more or less cancel out due to a possible spinning motion of the target. Moreover, a linear interpolation was employed for intermediate values of $\zeta$.

While the imparted momentum was computed directly in EXPEDIT, we used the average of the incident laser energy $\langle E_{\mathrm{inc}} \rangle$ to derive laser-induced heat from the parametric fit functions shown in Figure 2b. Accordingly, the average fluence is given by $\langle \Phi_{\mathrm{inc}} \rangle = \langle E_{\mathrm{inc}} \rangle / A_{\mathrm{cs}}$ where $A_{\mathrm{cs}}$ is the optical cross-section of the target. Admittedly, this approach discards the effects of oblique light incidence on the fluence and can only serve as a rough proxy. Nevertheless, it gives a good idea about thermo–mechanical constraints, which would have to be revised anyway once detailed knowledge on target shape and surface material is available.

However, this approach only holds true for sufficiently small targets where substantial outshining occurs. Larger targets with an optical cross-section that exceeds the beam spot size, $A_s < A_{cs}$, allow for an even more simplified computation using $\langle \Phi_{inc} \rangle = E_T / A_s$ where $E_T$ is the laser pulse energy arriving in orbit after atmospheric attenuation. With small targets and $A_{cs} < A_s$, however, computation via $\langle \Phi_{inc} \rangle = \langle E_{inc} \rangle / A_{cs}$ is chosen since this accounts for effects stemming from the spatial distribution of the fluence, assuming that the target is centered in the high-fluence area of the laser spot.

### *2.5. Prediction of Orbit Modification*

For the calculation of a direct station transit, the component $\Delta p_{ax}$ of the laser-imparted momentum vector, which is aligned co-axial with the laser beam propagation axis and can be taken from the above-mentioned database, can be separated into two subcomponents, namely imparted in-track momentum $\Delta p_t = \Delta p_{ax} \cdot \cos\beta$ and radial impulse transfer $\Delta p_r = \Delta p_{ax} \cdot \sin\beta$ where $\beta(t)$ is the angle of attack, cf. Figure 1. As indicated there, two different options for perigee lowering were assessed: In perigee lowering by head-on momentum, the object is only irradiated during its approach to the laser station, cf. Figure 1a. The main idea here is to decelerate the target by applying a tangential thrust opposite to the direction of motion. Therefore, the target irradiation had been quit from the point at which its elevation angle started to decrease, as this would lead to unwanted acceleration. In addition to tangential deceleration, the radial momentum components were considered for the computation of the modified orbit as well.

As a second option for irradiation, the scope of outward momentum, cf. Figure 1b is to increase the apogee altitude by additional radial momentum while at the same time lowering the perigee altitude. In contrast to head-on momentum, only the imparted radial momentum is used to compute perigee lowering by outward momentum. Imparted in-track deceleration from irradiation during the ascending segment of the pass can simply be compensated for by acceleration during the same interval of elevation angles of the descending transit period.

For the computation of orbit modification, we used the semi-latus rectum $q = a\left(1 - e^2\right)$ of the elliptical orbit to express the tangential component $v_t$ of the debris velocity $v = \sqrt{v_t^2 + v_r^2}$ by

$$v_t = \sqrt{GM/q}[1 + e\cos\varphi] \tag{8}$$

and the radial component $v_r$ via

$$v_r = \sqrt{GM/q}[e\sin\varphi] \tag{9}$$

where $a$ is the orbit's semi-major axis, $GM = 398600.4\ \mathrm{km}^3/\mathrm{s}^2$ is Earth's gravitational constant, $e$ is the numerical eccentricity of the orbit, and $\varphi$ is the true anomaly [40].

The change of the orbital parameters by laser-induced momentum from a station transit is given by [41]

$$\Delta e = [2(e_0 + \cos\varphi_0)\Delta v_t - r_0 \sin\varphi_0 \cdot \Delta v_r / a_0] / v_0 \tag{10}$$

$$\Delta a = 2a_0^2 v_0 \Delta v_t / GM, \tag{11}$$

where the subscript 0 denotes the orbital parameters before irradiation. From this, the change of the perigee radius can be computed using $r_p = (1 - e) \cdot a$ via

$$\Delta r_p = (1 - e_0)\Delta a - (a_0 + \Delta a)\Delta e. \tag{12}$$

For the irradiation pass, we used the mean altitude of the debris object and propagated the target's motion on a corresponding circular orbit, which is a good approximation for $\varphi_0 \approx 270^\circ$, cf. Equation (8), and, in our case, typically low values for $e$, cf. Equation (9). From Equations (10)–(12), it can be taken that in the case of the outward momentum approach, where $\Delta v_t = 0$, the minimum $\Delta r_p$, i.e., the maximum perigee lowering can be achieved for $\varphi_0 = 270^\circ$. Hence, it would be optimal to irradiate the object at a mean altitude when it descends apogee to perigee. If, instead, the average altitude on the ascending orbital path, i.e., $\varphi_0 = 90^\circ$ was chosen, the apogee would be lowered, and the perigee would be raised counterproductively.

In the head-on momentum approach, $\Delta v_t < 0$, the selection of the optimum true anomaly for irradiation is significantly more complex since it additionally depends on the eccentricity. While this optimization is beyond the scope of our study, we restrained our simulations to $\varphi_0 = 270^\circ$ for head-on irradiation. Note that for the sake of simplicity, the laser-imparted momentum components of all $N$ laser pulses are straightforwardly summed up and attributed to the orbital point with $\varphi_0 = 270^\circ$, i.e., we have

$$\Delta v_t = \sum_{i=1}^{N} \left\| \Delta \vec{v}_{t,i} \right\| \tag{13}$$

and

$$\Delta v_r = \sum_{i=1}^{N} \left\| \Delta \vec{v}_{r,i} \right\|. \tag{14}$$

While the former equation for the cumulative deceleration is intuitive from Figure 1, the latter might appear questionable regarding the related error due to the different directions and positions of $\Delta \vec{v}_{r,i}$ during the station pass. However, regarding the irradiation intervals employed in our study, cf. Section 3.1.2, we have only a small range of true anomalies during the pass, $\Delta\varphi = 5.2^\circ \pm 0.4^\circ$ for head-on irradiation and $\Delta\varphi = 7.8^\circ \pm 0.7^\circ$ for outward pointing. Hence, the angular variation of $\Delta \vec{v}_{r,i}$ is rather marginal. Moreover, the mean true anomaly in head-on irradiation is at $\varphi = 266^\circ \pm 0.3^\circ$, which is very close to $\varphi_0 = 270^\circ$.

## 3. Results

### *3.1. Laser Irradiation Settings*

### 3.1.1. Laser Fluence

It can be seen in Figure 4 that with our approach for turbulence compensation, the threshold fluences for laser ablation of aluminum and steel, which are at 1 to 2 J/cm$^2$, correspond to a beam diameter of 2–3 m, cf. Figure 2a can be exceeded at any orbit altitude considered in our study sufficiently well. In particular, for the highly frequented altitudes around 800–1000 km, optimum momentum coupling, occurring from around 3 to 7 J/cm$^2$, equivalent to beam diameters down to 1 m, can be achieved for a wide range of beam pointing zenith angles. At higher altitudes, certain restrictions exist for large zenith angles due to the great distance to the target and the correspondingly decreasing focusability of the beam, while at lower altitudes, the momentum coupling coefficient even decreases for small zenith angles due to the high fluences where plasma shielding starts to occur. Most likely, however, this would not be a reason to defocus the beam since the overall imparted momentum would still increase nearly proportional to the incident laser energy since $\Delta p = c_m \cdot E_{\text{inc}}$ and, in general, the effective fluence on the surface might be lower due to oblique beam incidence.

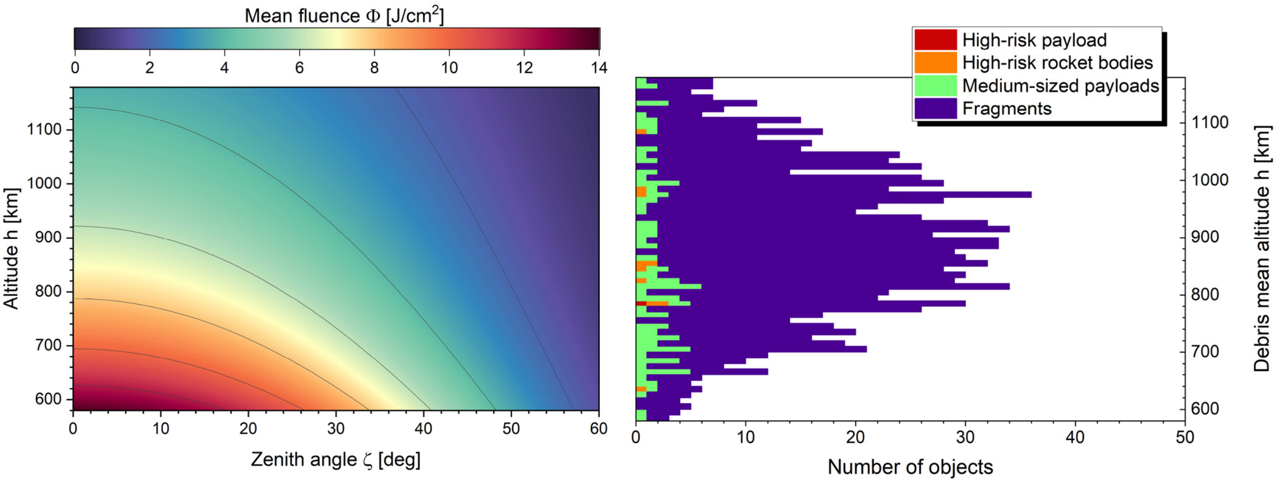

(**a**) (**b**)

**Figure 4.** (**a**) Mean fluence in the low Earth orbit (LEO) from a ground-based laser station using coherent coupling of 5000 laser emitters at 20 J pulse energy each. Laser wavelength $\lambda$ is 1030 nm, transmitter aperture: $D_{\mathrm{T}} = 4$ m. Turbulence compensation is employed using a laser guide star and phase control. (**b**) Occurrence of the selected 1111 debris objects.

### 3.1.2. Irradiation Interval

The efficiency of momentum generation strongly depends on the irradiation geometry during the station pass of the debris target. For head-on momentum, irradiation under low elevation angles is more beneficial than at small zenith angles regarding the in-track projection $\Delta p_t$ of the imparted momentum component, cf. Figure 5a. However, as can be seen from Equation (1), beam transmission constraints, in principle, lead to a larger spot size at greater distances between laser and target, which is the case at low elevation angles. In turn, the risk of energy losses by outshining the target increases; moreover, the fluence is significantly lower than at the zenith. Hence, obtaining the maximum in-track momentum comes as a trade-off between momentum projection and laser spot size, while radial momentum approaches its maximum for small zenith angles for both geometric as well as beam propagation reasons, cf. Figure 5b.

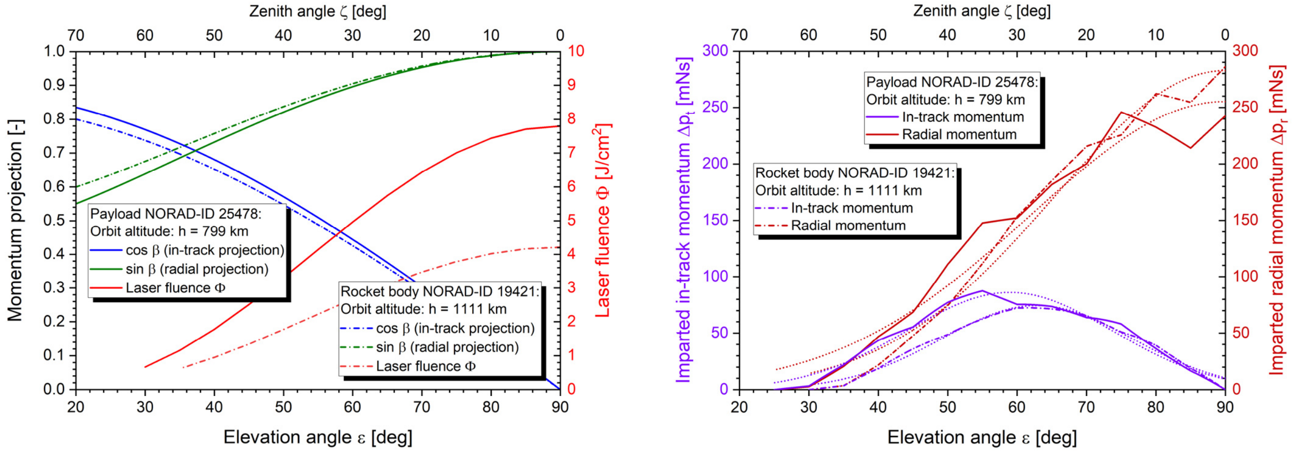

(**a**) (**b**)

**Figure 5.** Aspects of momentum changes in laser-based orbit modification for two debris target examples: (**a**) in-track (cos β) and radial (sin β) projection of momentum and laser fluence corresponding to the respective distance between laser and target, (**b**) imparted in-track and radial momentum per laser pulse. Dotted lines indicate Gaussian fit functions of the imparted momentum; see text.

Considering the risk of overheating the target, a restriction of the irradiation interval appears to be reasonable in order to avoid laser heating at fluences where the outcome in terms of momentum transfer is rather low. Hence, the magnitude of momentum transfer has been analyzed for the simulated targets at their different altitudes, and a Gaussian has been fitted to the data of momentum as a function of the zenith angle for each target's pass, cf. Figure 5b. The related fit parameters show a clear dependency on the orbit altitude, which makes sense from a geometric viewpoint. From the Full Width at Half Maximum (FWHM) of the Gaussian fit functions, averaged over the different target categories, we have determined the laser irradiation interval by the parameters shown in Table 1. They allowed us to derive the optimum onset angle $\zeta_{\mathrm{in}} = y_1 + m_1 \cdot h$ and termination angle $\zeta_{\mathrm{out}} = y_2 + m_2 \cdot h$ for head-on irradiation from the object's orbital altitude $h$. In the case of employing an outward irradiation approach, a symmetric interval has been chosen, i.e., $\zeta_{\mathrm{in}} = -\zeta_{\mathrm{out}} = y_3 + m_3 \cdot h$.

**Table 1.** Fit parameters for determination of the optimum laser irradiation interval of space debris using a pulsed laser at $\lambda = 1030$ nm, $\tau = 5$ ns, and $E_{\mathrm{L}} = 100$ kJ. Note that due to the strong non-linearity of $c_m$ removal of laser stations with deviating laser parameters or other power beaming performance likely demand different settings of the irradiation interval.

| **Category** | $y_1$ [°] | $m_1$ [°/km] | $y_2$ [°] | $m_2$ [°/km] | $y_3$ [°] | $m_3$ [°/km] |
|---|---|---|---|---|---|---|
| Payload | 59.9 | −0.0145 | 17.4 | −0.0052 | 41.1 | −0.0105 |
| Rocket Body | 68.7 | −0.0253 | 22.9 | −0.0099 | 54.2 | −0.0237 |
| Payload fragment | 55.7 | −0.0113 | 13.1 | −0.0024 | 34.6 | −0.0056 |
| Rocket fragment | 57.0 | −0.0158 | 14.9 | −0.0046 | 36.5 | −0.0092 |

### 3.1.3. Laser Pulse Repetition Rate

As a starting point for our analysis of orbit modification within a single station transit, we selected a laser pulse repetition rate of $f_{\mathrm{rep}} = 100$ Hz during the irradiation interval specified in Table 1. However, the resulting number of laser pulses will presumably be too large in terms of laser-induced heat deposition and potential loss of the target's mechanical integrity, which would eventually worsen the space debris situation. To assess this assumption, we analyzed fragments and mechanically intact targets separately regarding their thermal constraints.

Concerning the fragments, overheating might eventually lead to uncontrolled target melting and subsequent sphere formation from the initially typically rather flat shape, i.e., yielding a significantly lower optical cross-section and, hence, area-to-mass ratio, which might be detrimental to object tracking and removal [16]. Thus, in order to derive an upper limit for the repetition rate in the irradiation interval, we analyzed target heating at a 100 Hz repetition rate, cf. Section 2.4. In order to simplify subsequent downscaling of the laser repetition rate, for this computation, the enthalpies of fusion and vaporization have been discarded, and the material's specific heat has been assumed constant at its value at room temperature. Moreover, an initial temperature of 273.15 K before laser irradiation has been chosen, discarding the fluctuations of debris temperature during the orbital path through sunlight and Earth's shadow. Finally, we assumed that heat distributes sufficiently rapidly to achieve a uniform temperature distribution throughout the target before the next laser pulse arrives, which, at least for thin metal fragments, appears reasonable regarding their high heat conductivity.

It can be seen from the simulation results shown in Figure 6 that the target's temperature after irradiation increases linearly with its area-to-mass ratio, which can be deduced from Equation (7) yielding $T_{\mathrm{f}} \approx T_0 + (A/m)(1/c_p)\sum_i^N \eta_{res}(\Phi_i) \cdot \Phi_i$ where $\Phi_i$ is the fluence at the target surface at the $i$th pulse, $N$ is the number of laser pulses during the station pass, and the heat capacity is assumed to be constant such that $\Delta T = \eta_{res} E_{\mathrm{L}} / (m \cdot c_p)$ holds. The scatter in the depicted data stems from the various altitudes of the different targets, which affect the number of applied pulses, which increases with orbit height by up to more than 80% within the considered altitude range. Moreover, the achievable fluence at higher altitudes is considerably lower, cf. Figure 5a, which implies a stronger thermal coupling, cf. Figure 2b.

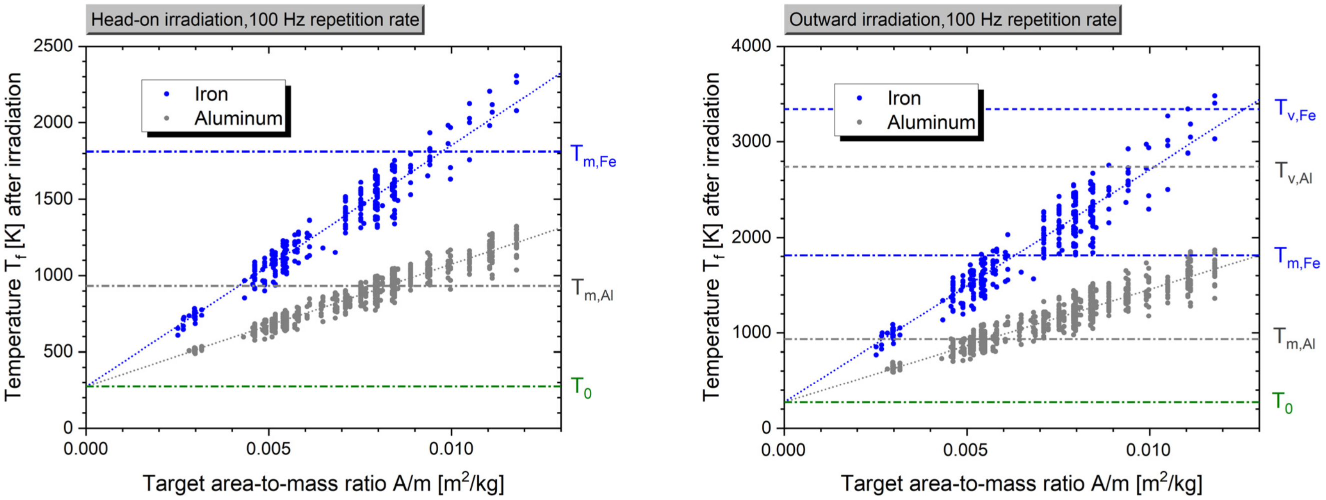

(**a**) (**b**)

**Figure 6.** Simulated temperature of space debris fragments after irradiation by a 100 kJ high-energy laser at 100 Hz pulse repetition rate during the zenith angle range as specified in Table 1 for (**a**) head-on and (**b**) outward irradiation, respectively.

Overall, it is evident that the number of laser pulses has to be limited to avoid the melting or even the vaporization of the target, in particular when their area-to-mass ratio is rather high. For that purpose, we decided to leave the angular irradiation range unchanged but to reduce the pulse repetition rate, which approximately decreases the temperature increment after the pass by the same amount. Choosing a pulse repetition rate of 9 Hz in the case of head-on irradiation and 6 Hz for outward irradiation yields a maximum temperature increment of $\Delta T \approx 100$ K for aluminum fragments with a very high area-to-mass ratio and $\Delta T \approx 200$ K for the respective fragments when the iron is considered as the target material. This temperature increment is less than 20% of the temperature increase necessary for target melting and seems to be a reasonable limitation of the repetition rate. After the irradiation, the acquired heat can be re-radiated into space to allow the target to cool down before its trajectory is modified further in a posterior laser station pass.

This assessment of thermal constraints does not hold for non-fragmented targets like payloads or rocket bodies, which are much more complex objects than a fragment that we consider homogeneous bulk material. Instead, the outer shell of such an object demands dedicated consideration. Even for a temperature increase to values substantially below the melting point, the deposited heat might already pose a high risk, e.g., in case stored energy, i.e., not completely discharged batteries or residual propellant, is located inside the object in the vicinity of an outer wall. Since these aspects were not available for a detailed assessment, we restrained our analysis to the computation of the average laser intensity during a station pass.

As an estimate for maximum permissible average irradiation intensity, we refer to [42], where an irradiance threshold for lethality against unhardened satellites significantly below 100 W/cm$^2$ was stated. Acknowledging that heat absorbance under laser ablation conditions might be significantly higher than for highly reflective metals, cf. Figure 2b, we chose $I_{\text{max}} = 13.7$ W/cm$^2$ as an upper limit for the average intensity during laser irradiation, which equals the hundredfold of the solar constant. To ensure that $I_{\text{max}}$ is not exceeded during irradiation, we set the repetition rate for outward irradiation altitude-dependent to $f_{rep}(h) = I_{max}/\Phi_0(h)$ where $\Phi_0$ is the laser fluence focused at a target with altitude $h$ in the zenith of the laser station, i.e., $\zeta = 0°$. Hence, the applicable laser repetition rate increases nearly linearly from 1.1 Hz at 600 km altitude to 3.8 Hz at 1200 km altitude.

While this limitation is reasonable for outward irradiation, where the object is irradiated during a relatively long timespan near the zenith, i.e., at high fluences, these values are reached merely at the end of the irradiation interval in the case of head-on irradiation. Therefore, we chose an enhanced repetition rate when computing the head-on momentum, which exceeded the repetition rate of outward irradiation at the respective altitude by 50%. While $I_{max}$ is hence exceeded at the end of the irradiation interval, this is somehow compensated since the arriving laser intensity is significantly lower in the initial phase of the irradiation interval—unlike in the case of outward irradiation, where high intensities are obtained for a relatively long timespan. Overall, this choice gives the same ratio of repetition rates as for fragments, where we had 9 Hz and 6 Hz, respectively. Hence, the selection of repetition rates should yield a nearly similar heat load ratio of the irradiated target for the different irradiation strategies.

## *3.2. Orbit Modification*

### 3.2.1. Orbital Velocity Changes

Figure 7a shows the simulation results for the resulting velocity changes of the debris objects when the restriction of the repetition rate to 6 and 9 Hz, resp., was applied. Again, a linear dependency of coupling on the object's area-to-mass ratio is found, which can be predicted from Equation (6) as $\Delta v = (A/m)\sum_{i=1}^{N} c_m(\Phi_i)\cdot\Phi_i$. However, the data on laser-induced velocity change exhibits a larger scatter than the data on temperature increment since, on top of the altitude dependency of pulse number and fluence, the different target shapes are reflected in the raytracing computation of imparted momentum as well. Overall, the resulting velocity change of a few m/s is about two orders lower than the required $\Delta v$ for perigee lowering of initially circular orbits for atmospheric burn-up, cf. [43], clearly indicating the necessity of debris irradiation during a multitude of station passes.

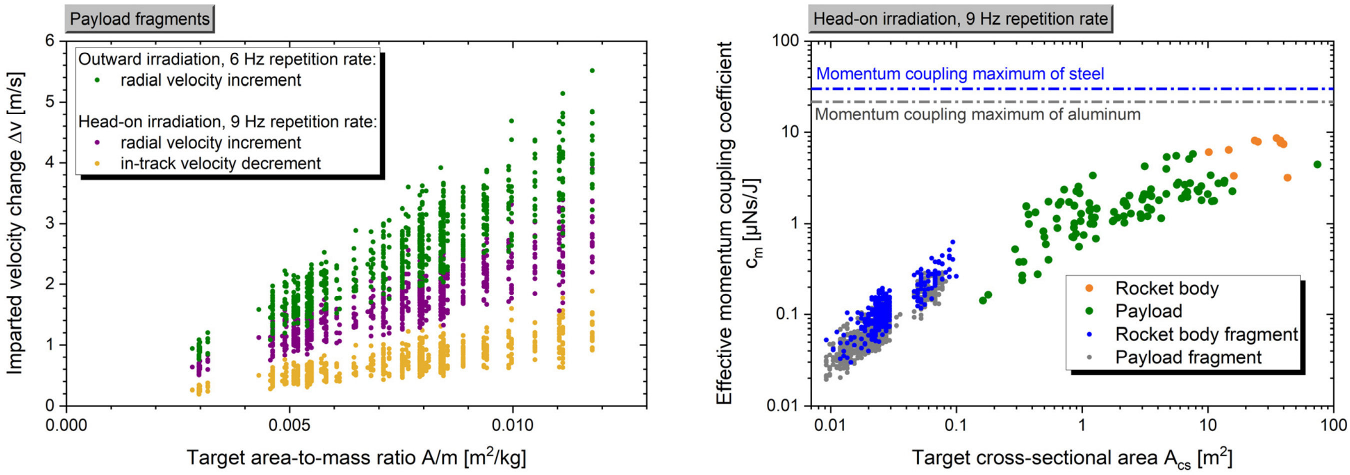

(**a**) (**b**)

**Figure 7.** Simulation results for (**a**) velocity change of aluminum fragments and (**b**) effective momentum coupling coefficient of different object types after repetitive head-on irradiation by a 100 kJ high-energy laser. Laser pulse repetition rates depend on target type and irradiation mode, cf. Section 3.1.3. The range of irradiation angles is defined in Table 1.

It should be noted here that the effective momentum coupling coefficient $c_{m,\text{eff}}$ significantly deviates from the experimental data on momentum coupling, as in Figure 2a. Here, we define $c_{m,\text{eff}}$ as a figure of merit for the entire debris removal system, i.e.,

$$c_{m,\text{eff}} = \sum \Delta v / \left(N_p \cdot E_L\right) \quad (15)$$

where $E_L$ is the initially emitted laser pulse energy and $N_p$ is the number of applied laser pulses. Accordingly, from Figure 7b, it can be taken that the effective momentum coupling is around two to three orders of magnitude below the experimental data, mainly due to the large outshining losses, in particular for small targets at beam diameters in the size range from 1 to 3 m. However, what seems here as a massive waste of laser energy is somehow needed for the small objects since the relatively large spot size enables momentum coupling to small objects even in the presence of a significant beam pointing jitter. In any case, the impact of outshining losses on the effective momentum coupling coefficient should be carefully considered in conceptual studies in order to avoid performance overestimation of any laser-based debris removal system.

### 3.2.2. Perigee Lowering Method

In the next step of our analysis, our findings on laser-induced velocity change from a station pass were employed to compute the corresponding perigee change of the respective target's orbit. The results of head-on irradiation are shown in Figure 8.

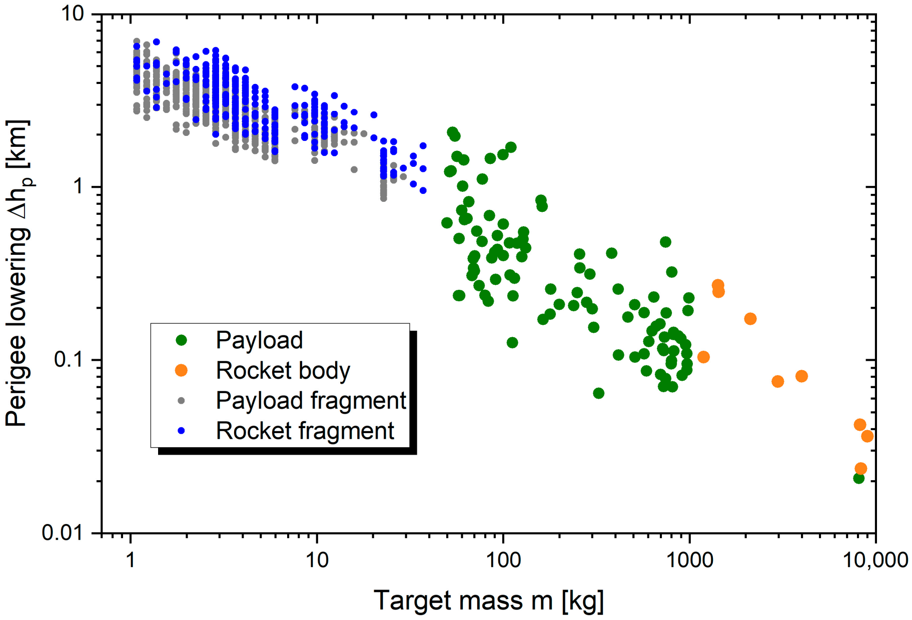

**Figure 8.** Simulation results on perigee lowering of space debris after a single station pass with head-on irradiation. Laser pulse repetition rates depend on the target type and irradiation mode, cf. Section 3.1.3. The range of irradiation angles is defined in Table 1.

Simulation results on perigee lowering after a transit with head-on irradiation are shown in Figure 8. Note that regarding the amount of perigee lowering, head-on irradiation outperforms outward irradiation by, on average, 23 ± 8%, even though the true anomaly for irradiation has not been optimized for head-on irradiation, cf. Section 2.5, and though outward irradiation benefits from lower zenith angles, i.e., higher fluences yielding an overall velocity change that exceeds the overall $\Delta v$ resulting from head-on irradiation by ca. 36 ± 5%.

Frequently, head-on irradiation is treated in the literature as pure deceleration, i.e., $v_r = 0$, and perigee lowering is computed using a Hohmann transfer from an initially circular orbit, i.e., assuming $e_0 = 0$ and $\varphi = \varphi_0 = 180°$, resulting in a required $\Delta v_t$ for perigee lowering, which is about four times lower than the needed $\Delta v_r$ in outward irradiation [43]. From our simulations, assuming $\varphi_0 = 270°$, we can see that in-track deceleration and imparted radial momentum contribute almost in equal parts to perigee lowering, in particular since the orbit's initial eccentricity is considered in our simulations. In conclusion, these findings disprove the view that head-on irradiation would be inefficient from the ground due to the large displacement between the laser source and orbital trajectory.

### 3.2.3. Multi-Pass Removal

From the results on perigee lowering in a single transit, a rough estimate can be given for the number $N_{\text{pass}}$ of required passes with laser irradiation to achieve the targeted perigee altitude of $h_{p,\text{final}} = 200$ km. For this purpose, the progress in the change of the orbit's eccentricity, semi-major axis, and perigee altitude has been monitored for a multitude of station transits until $h_p < h_{p,\text{final}}$. For the sake of simplicity, laser-imparted momentum has not been re-computed for each transit. Instead, the same $\Delta p$ was used for each pass, which means that for reasons of computational effort, we discarded the change $\Delta a$ of the mean altitude where the irradiation took place. Otherwise, a new set of laser–matter interaction tables would have to be computed for each target at every pass altitude, which would increase the overall computational effort of our study by several orders of magnitude. Moreover, we discarded the effects of mass loss following the findings in [39].

While discarding $\Delta a$ for momentum computation is no issue in outward irradiation where we have $\Delta v_t = 0 \Rightarrow \Delta a = 0$, cf. Equation (11), due to $\zeta_{\text{in}} = -\zeta_{\text{out}}$, for head-on irradiation, the mean altitude is lowered significantly in a single pass, approximately $\Delta a / \Delta r_p \approx 0.46 \pm 0.02$. Hence, higher laser fluence and less absolute hit uncertainty are obtained the more the perigee is lowered. Therefore, the number of required passes might, in principle, be overestimated while, on the other hand, better momentum coupling might as well be associated with higher thermal coupling—which in turn would demand for a stronger limitation of the number of laser pulses during a single transit at a lower altitude. Eventually, this might result in a similar overall efficiency of the laser irradiation during a single pass. At this point, a more precise assessment with more elaborate simulations has to be made in the future.

It can be seen from Figure 9a that the number of passes for lowering the perigee of fragments is, on average, 240 ± 130. The lowest numbers of transits are achieved for targets with a low initial perigee altitude and high area-to-mass ratio since a relatively small change of orbital velocity is needed, and a relatively large amount of laser energy can be captured for momentum transfer in this case.

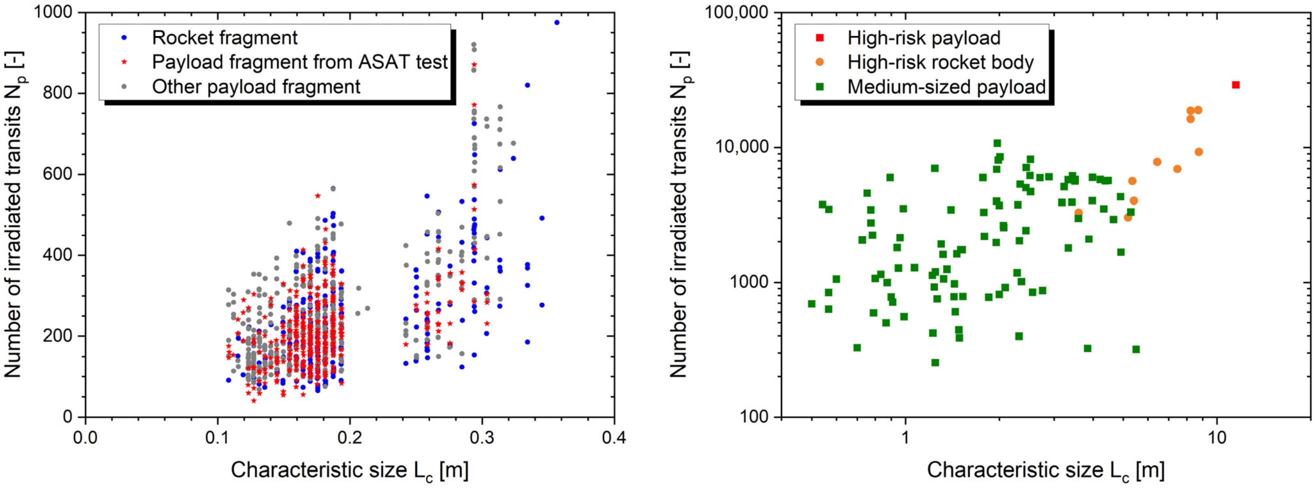

(**a**) (**b**)

**Figure 9.** Simulation results for the number of required passes for perigee lowering from LEO down to 200 km with head-on irradiation for (**a**) fragments and (**b**) non-fragmented debris objects.

In contrast, the resulting number of station passes with laser irradiation is relatively high for massive objects, as seen in Figure 9b. As the targets become significantly larger than the spot size, the ratio of spot area to target mass decreases strongly, thus, lowering the capability of laser-induced deceleration. With only a few exceptions, objects greater than 2 m demand more than 1000 passes with laser irradiation, while for the high-risk targets, between 3000 and 30,000 irradiations would be needed, which cannot be deemed a realistic perspective for their efficient removal at all. Therefore, it does not seem to be recommendable to remove larger objects using lasers unless they are rather lightweight and the required perigee lowering is not too large.

## 4. Discussion

### 4.1. Thermo—Mechanical Integrity

Thermo–mechanical limitations constitute rather tight constraints to laser-based orbit modification, which cannot be easily overcome. In contrast to earlier studies, e.g., [40], it can be stated that small space debris in LEO is not likely to be removed during a single pass, but irradiation during several passes has to be considered. It can be seen from Equations (6) and (7) that this is partly a material-specific issue and partly of technical nature: combining both equations, we obtain the thermo–mechanical coupling coefficient $c_{tm}$ [16]

$$c_{tm} = c_m / \eta_{res} \approx \frac{1}{c_p} \cdot \frac{\Delta v}{\Delta T} \tag{16}$$

representing the material's inherent thermal constraints for laser-based momentum change. From this viewpoint, optimizing orbit modification in a station pass would mean to maximize $c_{tm}$, eventually yielding a higher number of permissible laser pulses before thermal limits are met. In our case, this would simply mean maximizing the fluence even beyond the fluence where $c_m$ has its optimum since the benefit from the strong decrease in $\eta_{res}$ with the fluence predominates the performance loss of momentum coupling at high fluences, cf. Figure 2. In general, the selection of shorter laser pulse lengths could yield increased thermo–mechanical coupling coefficients as well, cf. [30], in particular when ultrashort pulses were used, as, e.g., proposed in [13] for space-based operation.

The heat deposited at the debris mainly depends on the number of laser pulses rather than the pulse repetition rate. Instead of choosing a low repetition rate, as undertaken in our study, the irradiation interval can also be shortened when higher repetition rates of 100 Hz and beyond are employed, which, however, might increase the requirements for target tracking due to rapid orbit modification. Note, however, that heat deposition can be significantly different for plastic fragments where high repetition rates might soon yield overheating and possible thermal decomposition of the irradiated surface due to low heat conductivities.

For mechanically intact objects, preservation of thermo–mechanical integrity is even more complex since our chosen limit of hundredfold solar irradiation is still rather generic. As an integral part of any removal procedure which employs high-energy laser radiation, a thorough and validated database of critical properties of such debris objects and their potential susceptibility to laser-induced thermo–mechanical stresses need to be in place, in particular regarding possible remainders of stored energy, in order to avoid fragmentation or, as a worst-case scenario, detonation from laser-heated propellant residuals. Moreover, certain components like solar panels, multilayer insulation (MLI), or components from carbon-fiber reinforced plastics (CFRP) might have to be excluded in general from pulsed laser irradiation due to fragmentation risks [17], eventually constraining laser-irradiation for removal to remainders from fragmentations but avoiding objects that have not fragmented (yet).

### 4.2. Momentum Prediction

Safety considerations are not limited to thermal constraints but need to cover dynamic issues as well. The dependency of velocity change on target size and area-to-mass ratio and, in particular, the significant scatter of $\Delta v$ due to the variety of different target shapes and materials, cf. Figure 7 underline that detailed target reconnaissance is mandatory for an accurate prediction of the modified trajectory to avoid harmful interference with other space missions. Moreover, we averaged over a multitude of Monte Carlo samples with different orientations, which rendered our method oblivious to the potentially large momentum scatter that might occur over time due to the object's rotational motion. Debris attitude analysis by lightcurve observations might prove to be game-changing for the selection of fortunate points of time where the laser-momentum coupling is both efficient and well predictable regarding magnitude and direction. Beyond the reconstruction of the rotational motion, information about the (predominant) debris material could be obtained from spectral [44] and polarimetric [45] analysis of the reflected light and eventually yield a better prediction of $\Delta v$ as well.

Overall, the predictability of momentum depends strongly on the ground station's performance of turbulence compensation and the remaining hit uncertainty from beam pointing jitter in combination with a priori uncertainty from target tracking. Together with the strong non-linearity of $c_m$ which is very sensitive to the incident fluence, cf. Figure 2a constitutes a significant risk of overestimating the achievable $\Delta v$ and its potential for optimization.

### 4.3. Removal Efficiency of Laser Station Networks

Incorporating the above-mentioned constraints like, e.g., thermo–mechanical integrity, hit uncertainty, and momentum non-linearity in our simulations, the resulting number of irradiations for removal, cf. Figure 9 shows a remarkable increase compared to earlier findings, e.g., in [15,39]. Moreover, in our study on irradiation of the debris, we have chosen a specific point of the trajectory, $\varphi_0 \approx 270^\circ$, where the induced orbit modification is rather fortunate for de-orbiting. In real-world scenarios, however, the apsidal line, which virtually connects apogee with perigee, naturally rotates over time, on average $2.3^\circ \pm 1.4^\circ$ per day for the initial orbits of our simulation targets, thus moving the optimum geographical latitude for laser irradiation continuously. Hence, a widespread distribution of the stations' geographical latitude might prove beneficial. Network simulations of multi-pass laser-based debris removal would yield a more profound assessment, including considerations of, e.g., the overall impact of non-direct station transit on in-track momentum reduction and the generation of cross-track momentum.

From earlier network simulations on photon pressure, we have already learned that a laser station network with only nine globally distributed sites would—under realistic weather conditions regarding laser access to the sky—be able to perform quasi-continuous laser tracking on a few-hourly or at least daily basis for approximately $N_{\mathrm{LXN}} \approx 1787$ debris objects in the low Earth orbit simultaneously [22]. Given the capacity of a station network to maintain a constantly updated "space debris laser catalog", adding high-energy laser pulses to each and every laser ranging maneuver would result in a continuous orbit modification of those cataloged objects. Therefore, in a very simplified and optimistic guess, we assume that such high-power irradiation could, in principle, be applied each time when it is required to re-evaluate orbital parameters to keep the object in the high-precision catalog, i.e., when the so-called laser tracking data expiry time $\tau_{\mathrm{LT}}$ has passed. Since irradiation would not be reasonable for every value of the true anomaly, cf. Equations (10)–(12) for the impact of $\varphi_0$ on $\Delta r_p$, we estimate the time between two removal irradiations to amount to at least $\Delta T = 2{\cdot}\tau_{\mathrm{LT}}$. From the number of required passes for perigee lowering, cf. Figure 9a one can compute that the average time needed to de-orbit a fragment would be around $340 \pm 240$ days. Therefore, as a rule of thumb, the average number of fragments that can be removed per year by such a network is slightly higher than the number of objects which can be simultaneously tracked by it, i.e., 1937 objects in our case.

Note that this is a rather rough assessment, and dedicated laser station network simulations on orbit modification would be needed to consolidate these numbers. Moreover, smaller fragments down to 1 cm in size might exhibit up to 50% higher area-to-mass ratio [38] than the smallest objects ($L_{c,\mathrm{min}} \approx 10.8$ cm) in our study yielding eventually a shorter time for de-orbit. Nevertheless, this network performance is about a factor of five times lower than the assumptions of [3] considering the laser-based removal of 100,000 small fragments in a time span of 10 years, which, hence, would require a significantly larger network of ground stations.

At this point, one can say that the continuing testing of anti-satellite weapons impedes all efforts for the protection of the space debris environment. Removing only the currently tracked fragments created from ASAT tests in space, namely 3472 objects [18], would already take more than a year with the above-mentioned laser network—not to mention the far greater number of smaller fragments not tracked yet.

## 5. Conclusions

Thermal constraints imposed by possible melt-up or fragmentation have a remarkable impact on the efficiency of laser-based debris removal by limiting laser pulse number and repetition rate for a single station pass. This has to be addressed thoroughly by well-defined irradiation maneuvers, shown exemplarily for our laser configuration with 100 kJ pulse energy at a wavelength of 1030 nm, where we had to restrict the pulse repetition rate to less than 10 Hz. This clearly renders debris de-orbiting within a single station transit unfeasible, and subsequent cooldown times in advance to the next laser station transit need to be incorporated into mission planning in order to ensure the mechanical integrity of the irradiated target to be maintained. From a different perspective, this statement illustrates the weaponization potential of this technology.

To ensure the operational safety of laser-based debris removal, remote reconnaissance of material, shape, temperature, and attitude is of great importance, allowing for a better assessment of the target's thermal limits as well as enabling a better prediction of the modified orbit. Moreover, not only momentum coupling but also thermo–mechanical integrity of space-aged targets under relevant laser irradiation conditions should be investigated experimentally to derive realistic estimates for the efficacy of laser-based removal, in particular regarding astrodynamic and atmospheric constraints.

Regarding sustainability in the Earth's orbital environment, high-power lasers might not be the optimum cure for the orbital disease from space debris, but—remaining in the picture of cure and disease—laser station networks could act very well as a needed painkiller significantly lowering the increasing burden of orbital collision avoidance and simultaneously supporting space sustainability by perceptibly reducing the large number of debris fragments which constitute centers of inflammation in the collisional cascade of the progressing Kessler syndrome. While high-power lasers do not appear particularly suitable for the removal of massive high-priority debris objects as the presumably most sustainable debris remediation step [6], they seem to be very well suited for massive removal of small debris, which is an increasingly emergent task.

**Author Contributions:** Conceptualization, J.K. and S.S.; methodology, J.K. and S.S.; software, J.K. and S.S.; validation, J.K. and S.S.; formal analysis, J.K. and S.S.; investigation, J.K. and S.S.; data curation, J.K. and S.S.; writing—original draft preparation, S.S.; writing—review and editing, S.S.; visualization, S.S. All authors have read and agreed to the published version of the manuscript.

**Funding:** This research was enabled by institutional funding.

**Data Availability Statement:** The data presented in this study are available from the corresponding author upon reasonable request. Debris data from the DISCOS database and debris population datasets from the Master-8 model are available from ESA upon reasonable request [37]. Conjunction data messages are not publicly available; however, TLE data can be accessed publicly [36].

**Acknowledgments:** Funding acquisition, resources provision, supervision, and project administration by Wolfgang Riede and Jochen Speiser are gratefully acknowledged. In addition to that, we thank our former students Jascha Wilken and Lukas Eisert for their great work in the development of the EXPEDIT software and, likewise, Erik Marten Klein regarding ablation modeling using COMSOL Multiphysics®. The debris simulation target catalog has been established in the study LARAMOTIONS, cf. [22], under contract 4000127148/19/D/CT. In particular, the compilation of debris fragments' mass and optical cross-section on Master-8 statistics by Christoph Bamann, formerly at TU Munich, Germany, now at Vyoma GmbH, is thankfully acknowledged. Moreover, the authors express thanks to ESA for data usage from DISCOS and Master-8 and to USSTRATCOM for making TLE data available. Language editing of the manuscript provided by Samantha Rose Siegert is gratefully acknowledged.

**Conflicts of Interest:** The authors declare no conflict of interest. The funders had no role in the design of the study; in the collection, analyses, or interpretation of data; in the writing of the manuscript; or in the decision to publish the results.

## References

1. Kessler, D.J.; Cour-Palais, B.G. Collision Frequency of Artificial Satellites: The Creation of a Debris Belt. *J. Geophys. Res.* **1978**, *83*, 2637–2646. [CrossRef]
2. Phipps, C.; Bonnal, C. Laser Ranging and Nudging in Space Debris Traffic Management. *Sens. Transducers J.* **2022**, *255*, 17–23. Available online: https://www.sensorsportal.com/HTML/DIGEST/P_3254.htm (accessed on 17 March 2023).
3. Colvin, T.J.; Karcz, J.; Wusk, G. *Cost and Benefit Analysis of Orbital Debris Remediation*; NASA Headquarters, Office of Technology, Policy, and Strategy: Washington, DC, USA, 10 March 2023.
4. Clearspace-1. Available online: https://www.esa.int/Space_Safety/ClearSpace-1 (accessed on 17 March 2023).
5. Astroscale Selects Rocket Lab to Launch Phase I of JAXA's Debris Removal Demonstration Project. Available online: https://astroscale.com/astroscale-selects-rocket-lab-to-launch-phase-i-of-jaxas-debris-removal-demonstration-project/ (accessed on 17 March 2023).
6. Liou, J.-C. An active debris removal parametric study for LEO environment remediation. *Adv. Space Res.* **2011**, *47*, 1865–1876. [CrossRef]
7. Johnson, N.L.; Krisko, P.H.; Liou, J.-C.; Anz-Meador, P.D. NASA's new breakup model of Evolve 4.0. *Adv. Space Res.* **2001**, *28*, 1377–1384. [CrossRef]
8. Acciarini, G.; Baresi, N.; Bridges, C.; Felicetti, L.; Hobbs, S.; Günes Baydin, A. Observation Strategies and Megaconstellations Impact on Current LEO Population. In Proceedings of the 2nd NEO and Debris Detection Conference, Darmstadt, Germany, 24–26 January 2023.
9. Hakima, H.; Emami, M.R. Assessment of active methods for removal of LEO debris. *Acta Astronaut.* **2018**, *144*, 225–243. [CrossRef]
10. Phipps, C.R.; Albrecht, G.; Friedman, H.; Gavel, D.; George, E.V.; Murray, J.; Ho, C.; Priedhorsky, W.; Michaelis, M.M.; Reilly, J.P. ORION: Clearing near-Earth space debris using a 20 kW, 530 nm, Earth-based, repetitively pulsed laser. *Laser Part. Beams* **1996**, *14*, 1–44. [CrossRef]
11. Schall, W. Orbital Debris Removal by Laser Radiation. *Acta Astronaut.* **1991**, *24*, 343–351. [CrossRef]
12. Phipps, C.R. L'ADROIT—A spaceborne ultraviolet laser system for space debris clearing. *Acta Astronaut.* **2014**, *104*, 243–255. [CrossRef]
13. Soulard, R.; Quinn, M.N.; Tajima, T.; Mourou, G. ICAN: A novel laser architecture for space debris removal. *Acta Astronaut.* **2014**, *105*, 192–200. [CrossRef]
14. Rubenchik, A.M.; Erlandson, A.C.; Liedahl, D. Laser system for space debris cleaning. *AIP Conf. Proc.* **2012**, *1464*, 448–455. [CrossRef]
15. Esmiller, B.; Jacquelard, C.; Eckel, H.-A.; Wnuk, E. Space debris removal by ground-based lasers: Main conclusions of the European project CLEANSPACE. *Appl. Opt.* **2014**, *53*, I45–I54. [CrossRef] [PubMed]
16. Scharring, S.; Lorbeer, R.-A.; Eckel, H.-A. Heat Accumulation in Laser-Based Removal of Space Debris. *AIAA J.* **2018**, *56*, 2506–2508. [CrossRef]
17. Loktionov, E.; Phipps, C.; Sharaborova, E. Unintended consequences with laser nudging or re-entry of satellites. *Acta Astronaut.* **2021**, *181*, 439–444. [CrossRef]
18. Weeden, B.; Samson, V. (Eds.) *Global Counterspace Capabilities: An Open Source Assessment*; Secure World Foundation: Broomfield, CO, USA, 2023.
19. Handmer, A. Lighting Up Down Under: A Science and Technology Studies examination of policy, legal and organizational challenges encountered during the development of Active Debris Removal technology in Australia. In Proceedings of the 73rd International Astronautical Congress (IAC), Paris, France, 18–22 September 2022.
20. Speiser, J.; Ewers, B.; Kästel, J.; Lorbeer, R.-A.; Oberbeckmann, D.; Sauder, D.; Weichelt, B. Thin Disk Laser Development for Space Debris Monitoring and Mitigation. In Proceedings of the 2022 Conference on Lasers and Electro-Optics (CLEO), San Jose, CA, USA, 15–20 May 2022.
21. Kästel, J.; Speiser, J. Turbulence Mitigation by Tiled Aperture Coherent Coupling of Laser Emitters. In Proceedings of the Laser Congress 2019 (ASSL, LAC, LS&C), Vienna, Austria, 29 September–3 October 2019; OSA Technical Digest, paper JW2A.44. Optica Publishing Group: Washington, DC, USA, 2019. [CrossRef]
22. Scharring, S.; Dreyer, H.; Wagner, G.; Kästel, J.; Wagner, P.; Schafer, E.; Riede, W.; Bamann, C.; Hugentobler, U.; Lejba, P.; et al. LARAMOTIONS: A conceptual study on laser networks for near-term collision avoidance for space debris in the low Earth orbit. *Appl. Opt.* **2021**, *60*, H24–H36. [CrossRef] [PubMed]
23. Deng, Y.; Ji, X.; Li, X.; Wang, T.; Yu, H. Optimal momentum coupling between the ground-based laser impulse and space debris. *Appl. Phys. B* **2022**, *128*, 138. [CrossRef]
24. Tyson, R.K. *Principles of Adaptive Optics*, 4th ed.; CRC Press: Boca Raton, FL, USA, 2016.

25. Olivier, S.S.; Gavel, D.T. Tip–tilt compensation for astronomical imaging. *J. Opt. Soc. Am. A* **1994**, *11*, 368–378. [CrossRef]
26. McClatchey, R.A.; Fenn, R.W.; Selby, J.; Volz, F.; Garing, J. *Optical Properties of the Atmosphere*; Air Force Cambridge Research Laboratories: Bedford, MA, USA, 1972.
27. Opiela, J.N. A study of the material density distribution of space debris. *Adv. Space Res.* **2009**, *43*, 1058–1064. [CrossRef]
28. D'Souza, B.C. Development of Impulse Measurement Techniques for the Investigation of Transient Forces due to Laser-Induced Ablation. Ph.D. Thesis, University of Southern California, Los Angeles, CA, USA, 2007.
29. Scharring, S.; Wagner, G.; Kästel, J.; Riede, W.; Speiser, J. Ablative collision avoidance for space debris in the Low Earth Orbit by a single multi-kJ pulse from a ground-based laser. In Proceedings of the 2021 AMOS Conference Proceedings, Maui, HI, USA, 14–17 September 2021.
30. Scharring, S.; Eisert, L.; Lorbeer, R.-A.; Eckel, H.-A. Momentum predictability and heat accumulation in laser-based space debris removal. *Opt. Eng.* **2019**, *58*, 011004-1–011004-12. [CrossRef]
31. Klein, E.M. Simulation of Space Debris Heating in Laser-Ablative Orbit Modification Manouvers. Master's Thesis, Technical University of Braunschweig, Braunschweig, Germany, 2021.
32. Raciukaitis, G.; Brikas, M.; Gecys, P.; Gedvilas, M. Accumulation effects in laser ablation of metals with high-repetition-rate lasers. *Proc. SPIE* **2008**, *7005*, 725–735. [CrossRef]
33. Scharring, S.; Karg, S.; Lorbeer, R.-A.; Dahms, N.; Eckel, H.-A. Low-Noise Thrust Generation by Laser-Ablative Micropropulsion. In Proceedings of the 30th International Electric Propulsion Conference (IEPC), Kobe, Japan, 4–10 July 2015. paper IEPC-2015-143.
34. Orzi, D.J.O.; Alvira, F.C.; Bilmes, G.M. Determination of femtosecond ablation thresholds by using laser ablation induced photoacoustics (LAIP). *Appl. Phys. A* **2013**, *110*, 735–739. [CrossRef]
35. McKnight, D.; Witner, R.; Letizia, F.; Lemmens, S.; Anselmo, L.; Pardini, C.; Rossi, A.; Kunstadter, C.; Kawamoto, S.; Aslanov, V.; et al. Identifying the 50 statistically-most-concerning derelict objects in LEO. *Acta Astronaut.* **2021**, *181*, 282–291. [CrossRef]
36. United States Strategic Command (USSTRATCOM). Two-Line Element Orbital Data, USSTRATCOM 2019. Available online: https://www.space-track.org/ (accessed on 20 April 2023).
37. European Space Agency-European Space Operations Center (ESA/ESOC), Space Debris User Portal (DISCOS Database, Master-8 Model), ESA/ESOC. 2019. Available online: https://sdup.esoc.esa.int/ (accessed on 20 April 2023).
38. Krisko, P.H.; Horstman, M.; Fudge, M.L. SOCIT4 collisional-breakup test data analysis: With shape and materials characterization. *Adv. Space Res.* **2008**, *41*, 1138–1146. [CrossRef]
39. Liedahl, D.A.; Rubenchik, A.; Libby, S.B.; Nikolaev, S.; Phipps, C.R. Pulsed laser interactions with space debris: Target shape effects. *Adv. Space Res.* **2013**, *52*, 895–915. [CrossRef]
40. Phipps, C.R.; Baker, K.L.; Libby, S.B.; Liedahl, D.A.; Olivier, S.S.; Pleasance, L.D.; Rubenchik, A.; Trebes, J.E.; George, E.V.; Marcovici, B.; et al. Removing orbital debris with lasers. *Adv. Space Res.* **2012**, *49*, 1283–1300. [CrossRef]
41. Wen, Q.; Yang, L.; Zhao, S.; Fang, Y.; Wang, Y. Removing small scale space debris by using a hybrid ground and space based laser system. *Optik* **2017**, *141*, 105–113. [CrossRef]
42. Bloembergen, N.; Patel, C.K.N.; Avizonis, P.; Clem, R.G.; Hertzberg, A.; Johnson, T.H.; Marshall, T.; Miller, R.B.; Morrow, W.E.; Salpeter, E.E.; et al. Beam Material Interactions and Lethality. In Report to The American Physical Society of the study group on science and technology of directed energy weapons. *Rev. Mod. Phys.* **1987**, *59 Pt II*, S119–S143. [CrossRef]
43. Jumper, G.Y.; Holladay, J.J.; Wiechert, M.K.; Seggel, W.A. Impact of Thrust Alignment on Orbital Debris Removal by Ground-Based Lasers. *J. Spacecr. Rocket.* **2012**, *49*, 261–267. [CrossRef]
44. Nussbaum, M.; Schafer, E.; Yoon, Z.; Keil, D.; Stoll, E. Spectral Light Curve Simulation for Parameter Estimation from Space Debris. *Aerospace* **2022**, *9*, 403. [CrossRef]
45. Dianetti, A.D.; Crassidis, J.L. Space Object Material Determination from Polarized Light Curves. In Proceedings of the AIAA Scitech 2019 Forum, San Diego, CA, USA, 7–11 January 2019. paper AIAA 2019-0377. [CrossRef]